

SIMULATION OF TWO-PHASE FLOW PAST A VERTICAL SURFACE-PIERCING CIRCULAR CYLINDER

Bonguk Koo, Jungsoo Suh¹, Jianming Yang, and Frederick Stern

IIHR-Hydroscience & Engineering, University of Iowa, Iowa City, IA, 52242, USA

ABSTRACT

Large-eddy simulation of the flow past a surface-piercing circular cylinder is performed to investigate the effects of Reynolds and Froude numbers using a high fidelity orthogonal curvilinear grid solver. The present study extends and supports the conclusions of the precursory work for medium Reynolds and Froude numbers. Organized periodic vortex shedding is observed in deep flow. At the interface, the organized periodic vortex shedding is attenuated and replaced by small-scale vortices. The streamwise vorticity and outward transverse velocity generated at the edge of the separated region cause the weakened vortex shedding at the interface. The main source of the streamwise vorticity and the outward transverse velocity at the interface is the lateral gradient of the difference between the vertical and transverse Reynolds normal stresses.

INTRODUCTION

Two-phase flow past a vertical surface-piercing circular cylinder is relevant for many engineering applications. The air-water interface adds significant complications. The effects of the interface on the force distributions on the cylinder, vortex generation and turbulent structures, and vortex shedding, especially, their changes with the Reynolds (Re) and Froude (Fr) numbers are not well understood. A better understanding of these effects is also important for the cases when vortex- and wave-induced vibrations of the cylinder are to be considered.

Recently, the authors studied the effects of air-water interface on the vortex shedding from a vertical circular cylinder for medium Re and Fr cases [1] using a high-fidelity orthogonal curvilinear grid solver [2]. The present study extends and supports the conclusions of the precursory work for medium Re and Fr numbers. Simulations are performed for two-phase turbulent flow past a circular cylinder in a free stream with conditions based on the experiments of Chaplin

and Teigen [3]. The forces on the cylinder, air-water interface topology including run-up on the front face of the cylinder and the vortex shedding pattern behind the cylinder are compared with the data.

COMPUTATIONAL METHODS

The mathematical model and numerical method in the orthogonal curvilinear coordinates used in this study are the extension of CFDShip-Iowa version 6, a sharp interface Cartesian grid solver for two-phase incompressible flows recently developed at IIHR by Yang and Stern [4]. In this solver, the interface is tracked by a coupled level set and volume-of-fluid (CLSVOF) method [5]. A ghost fluid methodology is adopted to handle the jump conditions across the interface, where the density and surface tension effect are treated in a sharp way while the viscosity is smeared by a smoothed Heaviside function.

Mathematical Model

The governing equations are the Navier-Stokes equations for two-phase, immiscible, incompressible flows in the orthogonal curvilinear coordinate system. The continuity equation is given as follows:

$$\nabla(i)[u_i] = 0 \quad (1)$$

where u_i is the velocity in the orthogonal coordinate

ξ_i direction and $\nabla(i)[\bullet] = \frac{1}{J} \frac{\partial}{\partial \xi_i} \left[\left(\frac{J}{h_i} \right) \bullet \right]$ following Pope

[6]. The Jacobian of the coordinate transformation is defined

as $J = h_i h_j h_k$, and $h_i = \frac{\partial x_i}{\partial \xi_i}$ with x_i a Cartesian coordinate.

The momentum equations are written as follows:

¹Current affiliation: Nuclear Engineering & Technology Institute, South Korea

$$\begin{aligned} \frac{\partial u_i}{\partial t} + \nabla(j)[u_i u_j] - \frac{1}{\rho} \nabla(j)[\tau_{ij}] = -\frac{1}{\rho} \frac{\partial p}{\partial \xi(i)} + g_i \\ + H_j(i) \left[u_j u_j - \frac{\tau_{ij}}{\rho} \right] - H_j(i) \left[u_i u_j - \frac{\tau_{ij}}{\rho} \right] \end{aligned} \quad (2)$$

where ρ is the density, p is the pressure, t is the time, and g_i the gravity vector in the ξ_i direction. In addition,

$$H_i(j) = \frac{1}{h_j} \frac{\partial h_i}{\partial \xi_j} \quad \text{and} \quad \partial \xi(i) = h_i \partial \xi_i \quad \text{as in [6].} \quad \tau_{ij} \text{ is}$$

defined as follows:

$$\tau_{ij} = \mu \left[\frac{\partial u_i}{\partial \xi(j)} + \frac{\partial u_j}{\partial \xi(i)} - u_i H_i(j) - u_j H_j(i) + 2u_i H_i(l) \delta_{ij} \right] \quad (3)$$

where μ is the dynamic viscosity and δ_{ij} is the Kronecker delta function.

In large eddy simulation (LES), the small dissipative eddies are modeled by the SGS model whereas the large, energy carrying eddies are resolved by the spatially filtered Navier-Stokes equations. The Lagrangian dynamic Subgrid-scale (SGS) model based on Sarghini et al. [7] is adopted in present LES. Eq. (2) is rewritten as the following form:

$$\begin{aligned} \frac{\partial \bar{u}_i}{\partial t} + \nabla(j)[\bar{u}_i \bar{u}_j] - \frac{1}{\rho} \nabla(j)[\bar{\tau}_{ij}] = -\frac{1}{\rho} \frac{\partial \bar{p}}{\partial \xi(i)} + g_i \\ + H_j(i) \left[\bar{u}_j \bar{u}_j - \frac{\bar{\tau}_{ij}}{\rho} - \bar{\tau}_{ij} \right] - H_j(i) \left[\bar{u}_i \bar{u}_j - \frac{\bar{\tau}_{ij}}{\rho} - \bar{\tau}_{ij} \right] \end{aligned} \quad (4)$$

with $\bar{\tau}_{ij} = \mu \bar{S}_{ij}$ and $\bar{\tau}_{ij} = \nu_i \bar{S}_{ij}$, respectively. Hereafter the filtering sign for LES will be dropped for simplicity.

Interface Representations and Fluid Properties

The interface is represented by the level-set (LS) function which is corrected using the volume of fluid (VOF) function to enforce mass conservation. The LS function, ϕ , is defined as a distance function which is negative in the air, positive in the liquid, and zero at the interface. The VOF function, F , is defined as the liquid volume fraction in a grid cell that gives zero in the air, one in the liquid, and a value between zero and one in an interfacial cell, respectively.

The LS function and the VOF function are advanced using

$$\frac{D\phi}{Dt} = \frac{\partial \phi}{\partial t} + (\mathbf{u} \cdot \nabla) \phi = 0 \quad (5)$$

$$\frac{DF}{Dt} = \frac{\partial F}{\partial t} + (\mathbf{u} \cdot \nabla) F = 0 \quad (6)$$

respectively.

Each phase of constant density and viscosity can be defined using the LS function in the computational domain and sharp jumps of the fluid properties occur at the phase interface. In this study, the density keeps its sharp jump and the viscosity is smoothed over a transition band across the interface,

$$\begin{aligned} \rho = \rho_G + \rho_L - \rho_G H \phi \\ \mu = \mu_G + \mu_L - \mu_G H_\varepsilon \phi \end{aligned} \quad (7)$$

where the subscripts G and L represent gas and liquid phase, respectively, the stepwise Heaviside function is

$$H \phi = \begin{cases} 1 & \text{if } \phi \geq 0 \\ 0 & \text{if } \phi < 0 \end{cases} \quad (8)$$

and the smoothed Heaviside function is

$$H_\varepsilon \phi = \begin{cases} 1 & \text{if } \phi > \varepsilon \\ \frac{1}{2} \left[1 + \frac{\phi}{\varepsilon} + \frac{1}{\pi} \sin\left(\frac{\pi\phi}{\varepsilon}\right) \right] & \text{if } |\phi| \leq \varepsilon \\ 0 & \text{if } \phi < -\varepsilon \end{cases} \quad (9)$$

Numerical Method

The finite-difference method is used to discretize the governing equations on a general orthogonal curvilinear grid. A staggered variable arrangement is adopted, i.e., the contravariant velocity components u_i, u_j, u_k are defined at cell faces in the ξ_i, ξ_j, ξ_k directions, respectively, and all other variables are defined at cell centers. A semi-implicit time advancement scheme is used to integrate the momentum equations with the second-order Crank-Nicolson scheme for the diagonal viscous terms and the second-order Adams-Bashforth scheme for other terms. A four-step fractional-step method is employed for velocity-pressure coupling, in which a pressure Poisson equation is solved to enforce the continuity equation.

The convective terms are discretized using the fifth-order Hamilton-Jacobi Weighted-ENO (HJ-WENO) scheme and other terms are approximated using the second-order central difference scheme. A semi-coarsening multigrid solver from the HYPER library [8] is used for the pressure Poisson equation.

The LS advection equation is solved using the third-order TVD Runge-Kutta scheme [9] for time advancement and the fifth-order HJ-WENO scheme [10] for spatial discretization. To keep the LS function as a signed distance function, it has to be reinitialized after a certain time of evolution. The CLSVOF method [11] is used to re-distance the LS function and improve mass conservation properties of the LS method. In the CLSVOF method, the interface is reconstructed based on the

VOF function with the interface normal computed from the LS function. The level set field is then re-distanced to reflect the position of the reconstructed interface, which satisfies the volume conservation constraint. In the present study, the piecewise linear interface construction scheme for the VOF method presented by Gueyffier et al. [12] is used.

Computational Setup

Body-fitted cylindrical grids of $256 \times 128 \times 128$ (radial, arimuthal, vertical directions, respectively) were used for all cases, as shown in Table 1. The grid points were clustered near the surface of the cylinder to resolve the boundary layer and flow separation. Near the interface the grid was also refined to capture the interface deformation. The computational domain was set up such that the portions of cylinder in the water and air are of length $4D$ and $2D$ with D the cylinder diameter, respectively. For $Fr = 0$ case, the air part is removed and the free surface is treated as a rigid lid. The distance from the center of the cylinder to the outer boundary is $20D$ including a buffer zone as shown in Fig. 1.

All variables were non-dimensionalized with the diameter of cylinder, D and the freestream velocity, U_∞ and the two non-dimensional parameters, Froude number and Reynolds number, are defined as following:

$$Fr = \frac{U_\infty}{\sqrt{gD}}, Re = \frac{U_\infty D}{\nu} \quad (10)$$

As shown in Table 1, different Re and Fr cases were investigated and a constant ratio of Re and Fr of 2.79×10^5 was used, following Chaplin et al. [3].

No-slip boundary conditions were applied on the cylinder wall, while the slip boundary condition was adopted at the bottom and the top of the computational domain. The radial outer boundary was divided into inflow and outflow boundaries at $\theta = 90^\circ$ and $\theta = 270^\circ$, in which θ is the tangential angle starting from the downstream direction. As shown in Fig 1, a Dirichlet boundary condition and a convective boundary condition [13] were used for the inflow and the outflow, respectively. In the present simulation, a constant CFL number of 0.3 was used where the magnitude of the time step varied from 1×10^{-2} to $1 \times 10^{-3} D/U_\infty$ depending on the flow conditions.

Verification and Validation

The time histories of the drag coefficient (C_D) and lift coefficient (C_L) with the running mean of C_D are shown in Fig. 2. The drag and lift coefficients are defined the same as Suh et al. [1]. The statistically stationary state is defined using the convergence of the running mean from the time history of C_D . 16 vortex shedding cycles were used for statistics. Fig. 3 presents the FFT of the drag and lift coefficients for $Fr = 0.84$. The dominant Strouhal number for C_L with $Fr = 0, 0.20, 0.44, 0.84$ is 0.192, 0.190, 0.200, 0.210, respectively and this is corresponding to the Karman vortex shedding, however; a

wide range of frequencies are shown for C_D . The mean drag coefficients are given in Table 1 and they agree very well with experimental data from Chaplin et al. [3] and Zdravkovich [14]. Note that there is no available data for $Fr = 0$ and $Fr = 0.20$.

Fig. 4 shows the vertical profiles of the mean streamwise velocity at $x = 4.5$ and $y = 0$ for $Fr = 0$ to $Fr = 0.84$. Note there is no available reference data for present Reynolds numbers so the data from Inoue et al. [15] and Kawamura et al. [16] of $Re = 2.7 \times 10^4$ were compared. The present results with $Fr = 0.84$ agree with ones from Inoue et al. [15] and Kawamura et al. [16] and it is clearly shown that the mean streamwise velocity decreases near the interface. However, other Fr cases show no significant decrease of the mean streamwise velocity near the interface and smaller mean streamwise velocity is observed in deep flow.

Fig. 5 presents the mean interface elevation at two transverse planes for both $Fr = 0.44$ and $Fr = 0.84$ cases. The case with $Fr = 0.44$ has good agreement with the computation of $Fr = 0.50$ by Kawamura et al. [16] at both transverse planes. The results of the $Fr = 0.84$ case are also in good agreement with previous studies except for the under-prediction of the depression, which is also reported in Suh et al. [1]. The run-up height are shown in Table 1 and have good agreement with the results from the Bernoulli's equation ($Fr^2/2$).

The mean interface elevation for $Fr = 0.84$ is shown in Fig. 6 and compared with measurement of $Fr = 0.80$ by Inoue et al. [15]. Overall, the present results are in good agreement with previous study even though the current Re is higher.

OVERVIEW OF MEDIUM RE/FR SIMULATION

Suh et al. [1] investigated the flow past a surface piercing circular cylinder at $Re = 2.7 \times 10^4$ and $Fr = 0.8$ using large-eddy simulation with a level-set/ghost-fluid method for the sharp interface treatment of the air-water interface and a Lagrangian dynamic SGS model for the dynamic modeling of the eddy viscosity in inhomogeneous complex flows.

In deep flow, organized vortex shedding can be observed, while the organized large-scale vortex shedding disappears near the interface and only small-scale vortices appear mostly at the edge of the separation region. The shear layers from the two sides of the cylinder digress from each other and no longer interact in deep flow. Separation is delayed due to the reduced adverse pressure gradient by the negative interface elevation slope along the cylinder.

The distribution of the mean velocity near the interface is significantly changed from the deep flow. The centerline mean streamwise velocity at far wake is independent with Re , whereas it varies significantly in near wake area. The recirculation zone increases substantially as the profile approaches to the interfaces. The streamwise length of the recirculation region at the interface is more than three times of the deep flow recirculation area and the magnitude of far-wake velocity at the interface is also remarkably smaller than the deep flow region.

The pattern of the mean streamwise and transverse velocity profiles at the interface shows to be quite different from that in deep flow. The mean streamwise velocity profiles for the horizontal zones away from the interface is between low Re and high Re experiment studies, whereas the mean streamwise velocity at the interface shows significantly different profile with increased wake depth. As the interface approaches, the magnitude of the mean transverse velocity increases.

The increased width of the separated region and the attenuation of vortex shedding near the interface is generated by the streamwise vorticity and outward transverse velocity at the edge of the separated region. The lateral gradient of the difference between the vertical and transverse Reynolds normal stresses is responsible for the streamwise vorticity and outward transverse velocity generated at the interface. The term $\frac{\partial^2}{\partial y \partial z}(\overline{v'v'} - \overline{w'w'})$ from the mean streamwise vorticity transport equation is the main production mechanism for the mean streamwise vorticity. The vertical and transverse gradients of the difference between $\overline{v'v'}$ and $\overline{w'w'}$ are responsible for the generation of the streamwise vorticity near the interface and presumably cause the outward transverse velocity near the interface.

RESULTS AND DISCUSSIONS

Four different Re and Fr cases are simulated; however, the case with $Re = 2.34 \times 10^5$ and $Fr = 0.84$ is mainly presented and compared with previous computational studies by Suh et al. [1]. Note that present studies used Re in the subcritical regime (1,000 to 2×10^5) so that similar flow patterns were observed. Higher Re/Fr ($3.46 \times 10^5/1.24$ and $4.58 \times 10^5/1.64$) cases will be performed for further investigation.

Instantaneous Flow

Instantaneous vertical vorticity at different depth including the interface are shown in Fig. 7. In deep flow, organized vortex shedding is evident as shown in Fig.7 (c) and (d). However, small scale vortices appear at the interface instead of organized large vortex shedding. In addition, necklace vortices are observed in front of the cylinder for $Fr = 0.20, 0.44$ (not shown) and $Fr = 0.84$, which was also reported in Suh et al. [1]. The instantaneous vortical structures identified by the second invariant velocity gradient tensor was used to obtain further details on large-scale flow structures, as shown in Fig. 8. The vortical structures are inclined as the interface is approached for $Fr = 0.84$, while they are almost parallel to the cylinder wall for $Fr = 0, 0.20$, and 0.44 . This pattern is also shown in the vortex core lines and it will be discussed in later section.

Mean Flow

The friction and pressure coefficients at different depth for $Fr = 0.84$ are shown in Fig. 9. The boundary layer separation

point for deep flow is 0.462π which is exactly same as that from Suh et al. [1]. Near the interface, the separation occurs at 0.487π , whereas the separation takes place at 0.514π in the case of Suh et al. [1]. The pressure coefficient has good agreement with experimental data from Norberg [17] with $Re = 2 \times 10^5$ up to 0.4π . Near the interface the pressure coefficient is very different from the deep flow. The delayed separation point near the interface is due to the decreased adverse pressure gradient which comes from the negative interface elevation slope near the cylinder. And this was also observed in Suh et al. [1].

The sectional mean drag coefficient and rms of the lift coefficient for $Fr = 0.84$ are given in Fig. 10. The drag coefficient is in good agreement up to the interface; however there are differences under the interface. The maximum drag coefficient appears at the interface which was also reported by Suh et al. [1], whereas Chaplin et al. [3] showed the drag coefficient reaches maximum approximately $z = -0.5$. The rms of the lift coefficient approaches almost zero at the interface and this indicates the attenuation of vortex shedding at the interface [1].

The mean separation pattern with the vortex core lines, obtained from the approach discussed in Kandasamy et al. [18] and Sujudi and Haimes [19], is given in Fig. 11 for $Fr = 0.84$. The three different types of vortices defined in Suh et al. [1] are observed: mean vertical vortices (V1), mean streamwise vortices (V2), and V-shaped mean vortex inside the separation region (V3). In contrast, V2 and V3 do not appear in the $Fr = 0, 0.20$, and 0.44 and V1 is not attached to the cylinder wall and it is almost parallel to the cylinder wall as the interface is approached. As the Fr gets smaller, the separation region gets flatter. Details of these vortices are discussed in Suh et al. [1].

Fig. 12 presents the mean streamwise velocity on the centerline in the wake of the cylinder. All the mean velocity profiles except for at the interface agree with the measurements by Lourenco and Shih [20]. As approaching the interface, the recirculation region is dramatically increased and the mean velocity at far wake is much smaller, which was also observed by Suh et al. [1].

Fig. 13 shows the mean streamwise and transverse velocities at different depths in the wake of the cylinder for $Fr = 0.84$. The pattern of the mean streamwise and transverse velocity profiles at the interface is quite different from that in deep flow. In deep flow, the mean streamwise velocity profiles at both locations ($x = 1.06$ and $x = 2.02$) agree with the measurements by Lourenco and Shih [20], whereas at the interface it has substantially increased wake width. The maximum outward mean transverse velocity appears at the interface and a very small outward mean transverse velocity appears below the interface. Karman vortex shedding at the interface is attenuated due to this outward mean transverse velocity at the edge of the separated region, which was also mentioned by Suh et al. [1].

The mean velocity contours with path-lines at the interface are shown in Fig. 14. Substantial changes of the mean

streamwise velocity for $Fr = 0.84$ occur near the separation region, as shown in Fig. 14 (j). The outward mean transverse velocity for $Fr = 0, 0.20$ and 0.44 is smaller than that for $Fr = 0.84$, as shown in Fig. 14 (k). This was also reported by Suh et al. [1]. The mean vertical velocity near the separation region becomes negative, which indicates the decreased wave elevation in that region.

The mean streamwise velocity contours at two cross-stream planes in the near wake are shown in Fig. 15 (a) and (e). Only a half domain is shown and the location of the interface (dotted line) and the cylinder wall (solid and dot line) are shown. Negative mean streamwise velocity occurs near the interface and in deep water at $x = 1$ plane (recirculation region). However, at $x = 2.5$ plane, negative velocity presents only near the interface. The width of the wake is constant in deep flow at plane $x = 1$, whereas the wake width near the interface increases substantially.

The mean vorticity contours at two cross-stream planes at the near wake area are given in Fig. 15 (b) - (h). The streamwise vorticity is responsible for the large outward mean transverse velocity near the interface [1]. In addition, the vortex shedding near the interface is attenuated and the wake width increases remarkably near the interface due to the mean streamwise vorticity. The mean transverse vorticity occurs only near the interface at $x = 1$ and $x = 2.5$. This indicates that the transverse vorticity induces the interface fluctuations. The mean vertical vorticity at $x = 1$ has high magnitude near the interface and this corresponds to the high mean streamwise velocity gradients near the interface.

Reynolds Stress

Fig. 16 shows the Reynolds stresses at two cross-planes. At $x = 1$ plane, the streamwise Reynolds stress has high magnitude at the region below the interface where the high mean streamwise velocity gradients present and it is the indication of high turbulent energy production. At $x = 2.5$, similar pattern of magnitude appears near the interface; however; the magnitude decreases in deep flow. In the separation region, the transverse Reynolds stress reduces as approaching the free surface. The vertical Reynolds stress shows high magnitude at the interface and this plays an important role for the large changes of the streamwise vorticity and the outward transverse velocity at the interface. The Reynolds shear stress has a small magnitude at the free surface. Fig. 17 shows the contours of the vertical Reynolds stress at the interface. High gradient of the vertical Reynolds stress occurs in the region with a high outward transverse velocity. It indicates that the lateral gradients of the difference between the transverse and vertical Reynolds stress induce the streamwise vorticity and the outward transverse velocity, as proposed by Suh et al. [1].

CONCLUSIONS

The flow past a surface-piercing circular cylinder has been studied for Re and Fr effects using large-eddy simulation. The present study is an extension and supports the conclusions of a precursory study for medium Re and Fr simulations, which investigated the effects of air-water interface on the vortex shedding from a vertical circular cylinder [1]. Similar flow features have been obtained since the Reynolds numbers for current studies are in the subcritical regime ($Re = 1,000$ to 2×10^5).

Quasi-vertical vortices from the organized periodic vortex shedding present in deep flow. Organized large-scale vortex shedding is attenuated and only small-scale vortices appear at the interface. The vortex shedding attenuation at the interface is induced by the streamwise vorticity and outward transverse velocity generated at the edge of separated region. The lateral gradient of the difference between the vertical and transverse Reynolds stresses is responsible for the streamwise vorticity and outward velocity generated at the interface.

To systematically study the origin of the surface current, i.e., the outward transverse velocity at the interface, a series of cases at different supercritical Re/Fr ($3.46 \times 10^5/1.24$ and $4.58 \times 10^5/1.64$) reported in [3], will be simulated. The effects of Re/Fr on the flow, including forces/pressure/shear-stress distributions, turbulent structures, and vortex shedding, will be investigated in detail. Verification and validation studies will be done with systematic grid refinement. The effect of the interface density jump on vorticity transport will also be investigated. Further investigations will be performed to study the origin of the mean streamwise vorticity and the outward transverse velocity near the interface using the mean streamwise vorticity transport equations. Lastly, to obtain better understanding of vortex- and wave- induced vibrations, forced pure sway motion simulations will be conducted.

ACKNOWLEDGEMENTS

This work was supported by research grants N00014-01-1-0073 and N00014-06-1-0420 from the Office of Naval Research (ONR), with Dr. Patrick Purtell as the program manager. The simulations presented in this paper were performed at the Department of Defense (DoD) High Performance Computing Modernization Program (HPCMP) NAVO Computing Center.

REFERENCES

- [1] Suh, J., Yang, J., and Stern, F., 2009, "The Effect of Air-Water Interface on the Vortex Shedding from a Vertical Circular Cylinder," submitted Journal of Fluids and Structure.
- [2] Yang, J., Bhushan. S., Suh, J., Wang, Z., Koo, B., Sakamoto, N., Xing, T., and Stern, F., 2008, "Large-Eddy Simulation of Ship Flows with Wall-Layer Models on Cartesian Grids," 27th Symposium on Naval Hydrodynamics, October 2008, Seoul, Korea.

[3] Chaplin, J. R. and Teigen, P., 2003, "Steady Flow past a Vertical Surface-Piercing Circular Cylinder," *Journal of Fluids and Structure*, 18, pp. 271-285.

[4] Yang, J. and Stern, F., 2009, "Sharp Interface Immersed-Boundary/Level-Set Method for Wave-Body Interactions," *J. Comput. Phys.*, 228(17), pp. 6590-6616.

[5] Wang, Z., Yang, J., Koo, B. G., and Stern, F., 2009, "A Coupled Level Set and Volume-of-Fluid Method for Sharp Interface Simulation of Plunging Breaking Waves," *Int. J. Multi. Flow*, 35(3), pp. 227-246.

[6] Pope, S. B., 1978, "The Calculation of Turbulent Recirculating Flows in General Orthogonal Coordinates," *J. Comp. Phy.*, 26, pp. 197-217.

[7] Sarghini, F., Piomelli, U., Balaras, E., 1999, "Scale-similar Models for Large-Eddy Simulations," *Phy. Fluids*, 11(6), pp. 1596-1607.

[8] Falgout, R. D., Jones, J. E., Yang, U. M., 2006, "Numerical Solution of Partial Differential Equations on Parallel Computers. Vol. 51. Springer-Verlag, Ch. The design and implementation of HYPRE, a library of parallel high performance preconditions, pp. 267-208.

[9] Shu, C.W. and Osher, S., 1988, "Efficient Implementation of Essentially non Oscillatory Shock-Capturing Schemes," *J. Comput. Phys.*, 77(2), pp. 439-471.

[10] Jiang, G. and Peng, D., 1999, "Weighted ENO schemes for Hamilton-Jacobi equations," *SIAM Journal. on Scientific Computing*, 21(6), pp. 2126-2143.

[11] Sussman, M., Puckett, E. G., 2000, "A Coupled Level Set and Volume-of Fluid Method for Computing 3D Axisymmetric Incompressible Two-Phase Flows," *J. Comput. Phys.*, 162, pp. 301-337.

[12] Guyeffier, D., Li, J., Nadim, A., Scardovelli, S., Zaleski, S., 1999, "Volume of Fluid Interface Tracking with Smoothed Surface Stress Methods for Three-Dimensional Flows," *J. Comput. Phys.*, 152, pp. 423-456.

[13] Breuer, M., 1998, "Large Eddy Simulation of the Subcritical Flow past a Circular Cylinder: Numerical and Modeling aspect," *Int. J. Numer. Meth. Fluids*, 28, pp. 1281-1302.

[14] Zdravkovich, M. M., 1997, "Flow Around Circular Cylinder, Vol. 1: Fundamentals," Oxford University Press, New York.

[15] Inoue, M., Bara, N., Himeno, Y., 1993, "Experimental and Numerical study of Viscous Flow Field Around an Advancing Vertical Circular Cylinder Piercing a Free-Surface," *J. Kansai Soc. Nav. Arch.*, 220, pp. 57-64.

[16] Kawamura, T., Mayer, S., Garapon, A., Sørensen, L., 2002, "Large Eddy Simulation of a Flow Past Free Surface Piercing Circular Cylinder," *J. Fluids Engng.*, 124, pp. 91-101.

[17] Norberg, C., 1992, "Pressure Forces on a Circular Cylinder in Cross Flow," In: *IUTAM Symposium Bluff-Body Wakes, Dynamics and Instabilities*. Göttingen, Germany, pp. 275-278.

[18] Kandasamy, M., Xing, T., Stern, F., 2009, "Unsteady Free Surface Wave-Induced Separation: Vortical Structures and Instabilities," *J. Fluids and Struct.*, 25, pp. 343-363.

[19] Sujudi, D., Haines, R., 1995, "Identification of Swirling Flow in 3-D Vector Fields," *AIAA paper*, 95-1715.

[20] Lourenco, L. M., Shih, C., 1993, "Characteristics of the Plane Turbulent Near Wake of a Circular Cylinder. a particle image velocimetry study. Data taken from A.G. Kravchenko and P. Moin, 2000, "Numerical Studies of Flow over a Circular Cylinder at $Re_D=3900$," *Phy. Fluids*, 12(2), pp. 403-417.

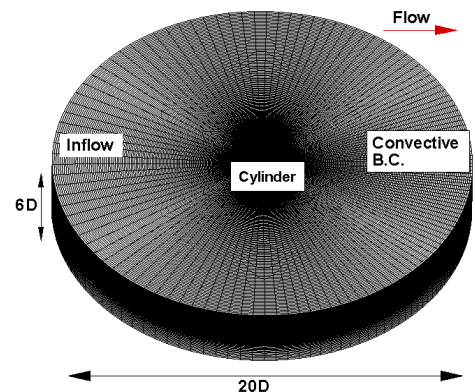


Figure 1 Computational domain with grid and boundary conditions

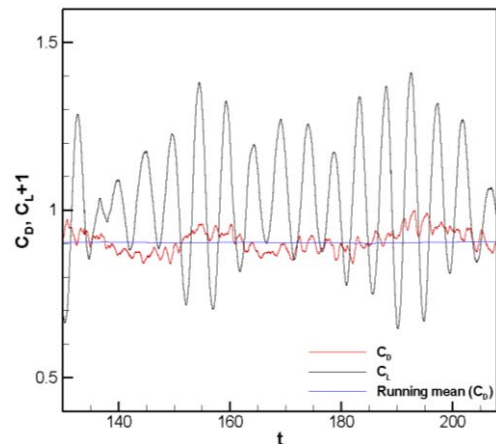


Figure 2 Time history and running mean for drag coefficient and time history for lift coefficient for $Fr = 0.84$.

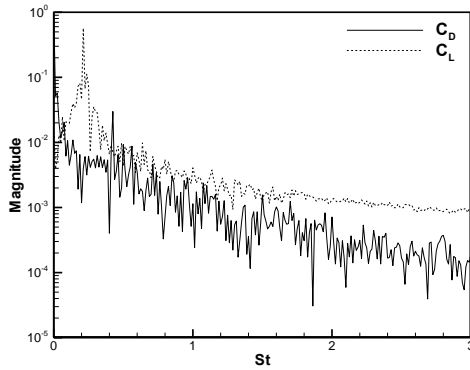


Figure 3 FFT of the drag and lift coefficient for $Fr = 0.84$.

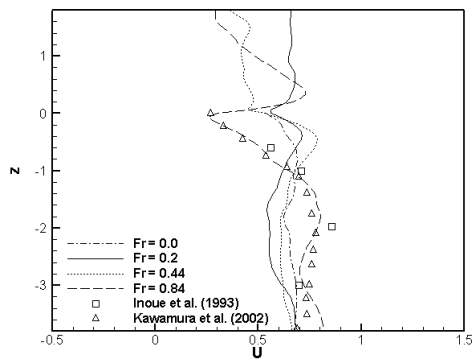


Figure 4 Vertical profiles of the mean streamwise velocity at $x = 4.5, y = 0.0$ for $Fr = 0, Fr = 0.20, Fr = 0.44,$ and $Fr = 0.84$.

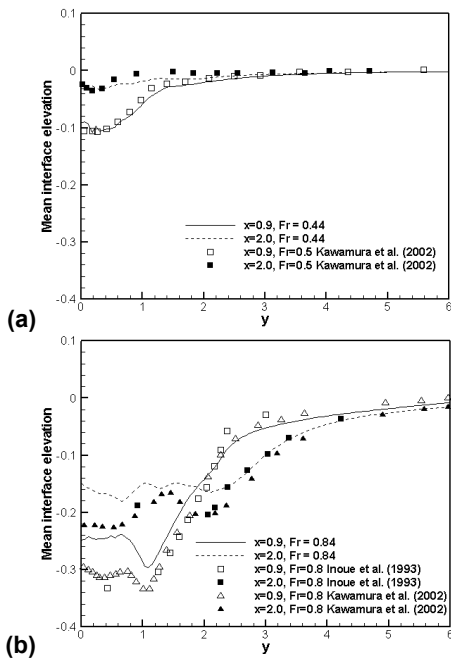


Figure 5 Profiles of mean interface elevation at $x = 0.9$ and $x = 2.0$. (a) $Fr = 0.44$; (b) $Fr = 0.84$.

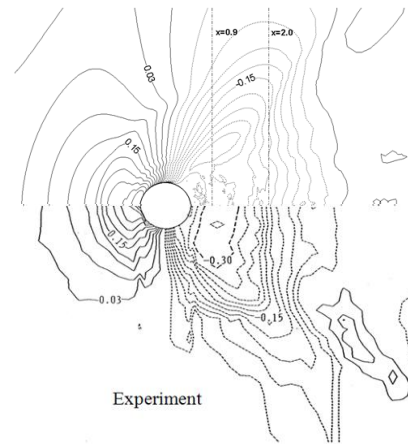


Figure 6 Mean interface elevation; Top: computation, $Fr = 0.84$; bottom: measurement by Inoue et al. (1993), $Fr = 0.8$

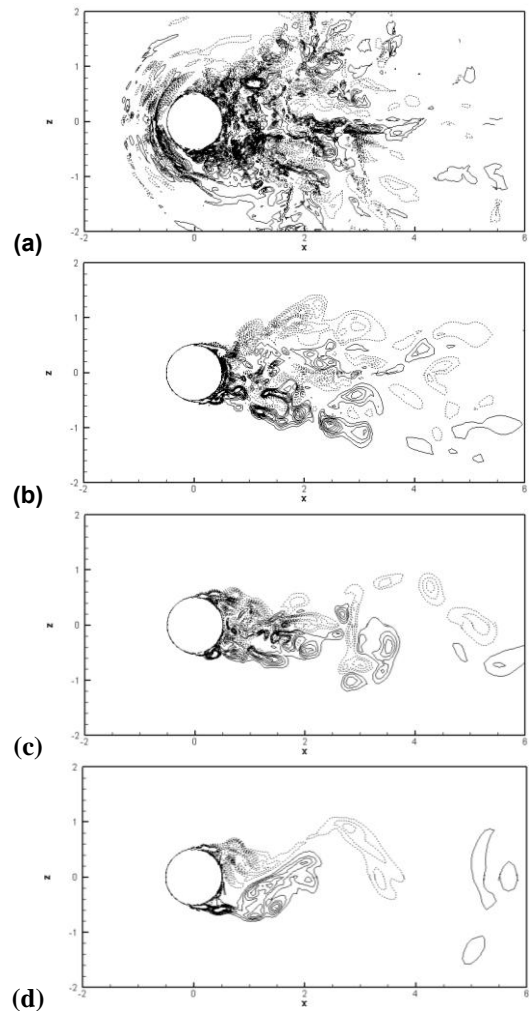


Figure 7 Instantaneous vertical vorticity at the interface and horizontal planes for $Fr = 0.84$. (a) On the interface; (b) $z = -0.5$; (c) $z = -1$; (d) $z = -3.5$. Contour interval is 1.2.

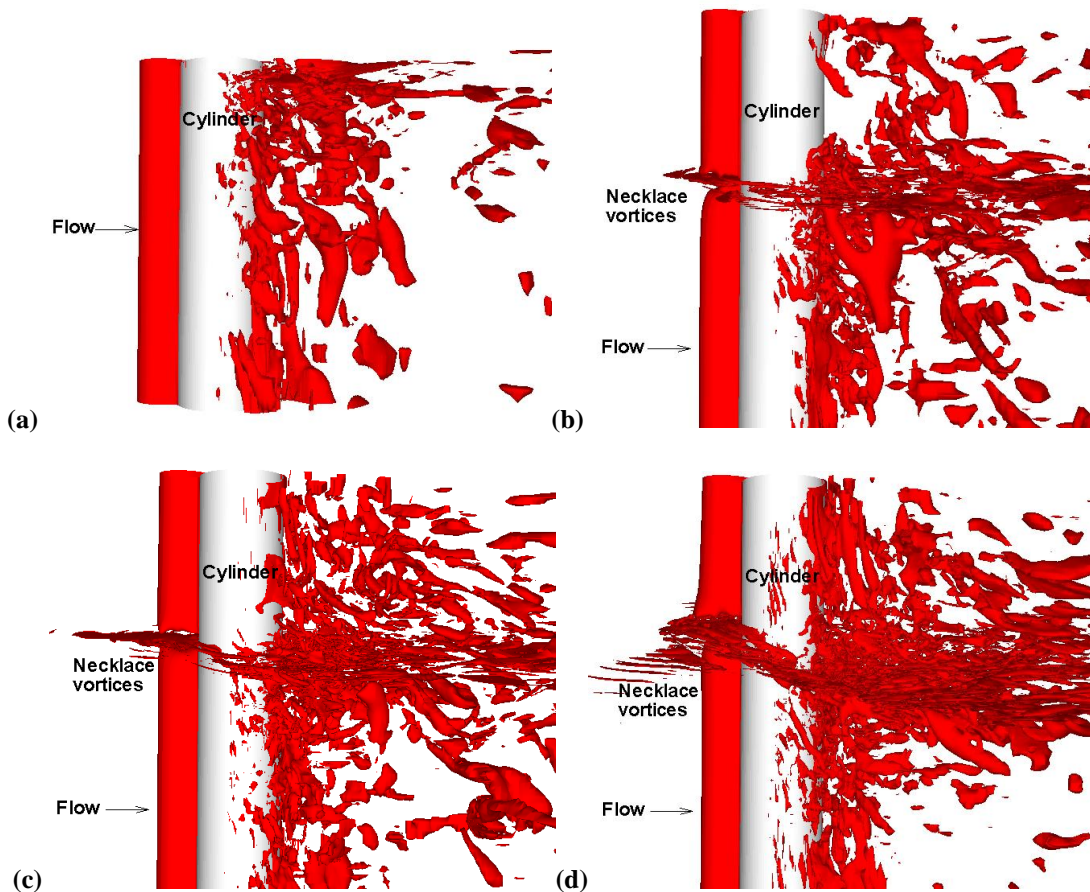


Figure 8 Instantaneous vertical structures identified by the second invariant of the velocity gradient tensor $Q = 0.5$ for (a) $Fr = 0$; (b) $Fr = 0.20$; (c) $Fr = 0.44$; (d) $Fr = 0.84$.

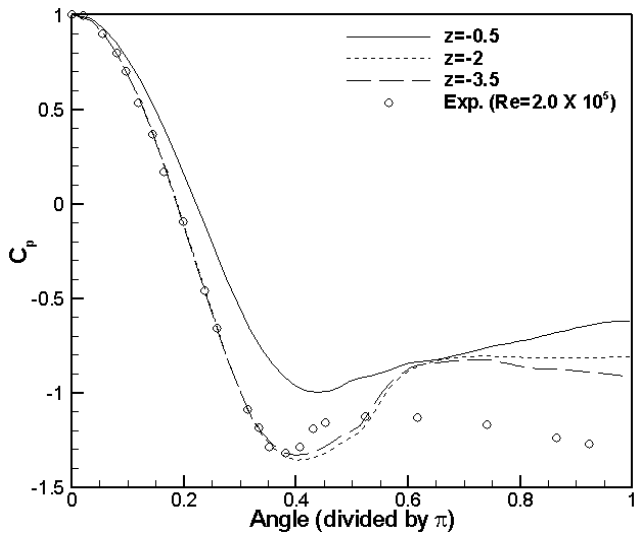


Figure 9 Pressure coefficient for $Fr = 0.84$

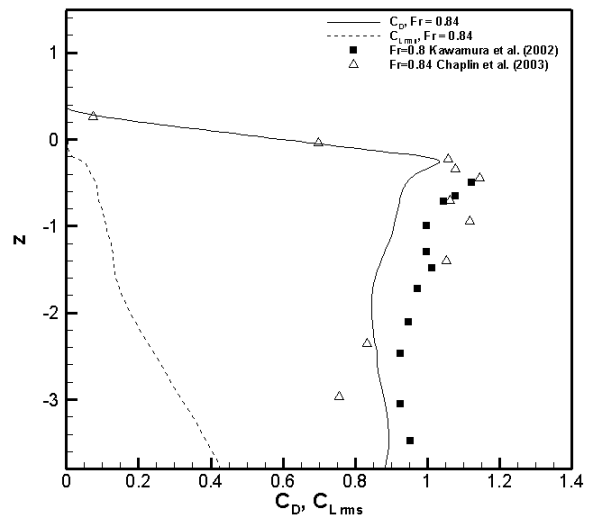


Figure 10 Sectional drag and lift coefficients for $Fr = 0.84$.

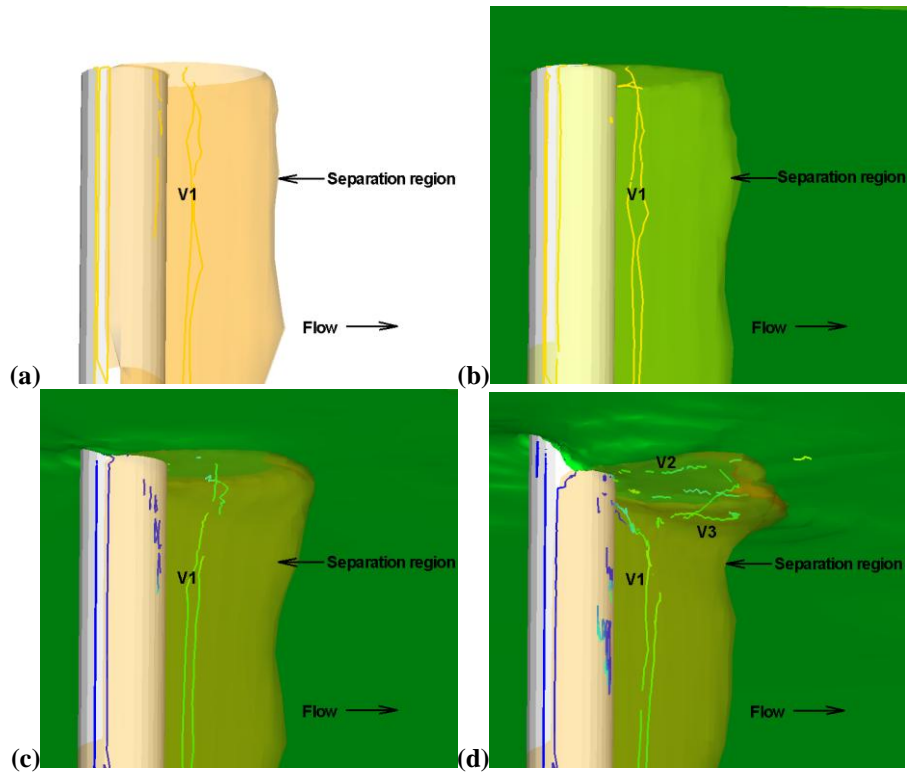


Figure 11 Mean separation pattern with vortex core lines for (a) $Fr = 0$; (b) $Fr = 0.20$; (c) $Fr = 0.44$; (d) $Fr = 0.84$.

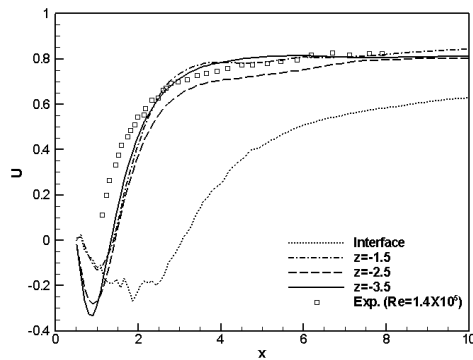


Figure 12 Mean streamwise velocity on the centerline in the wake of a circular cylinder for $Fr = 0.84$.

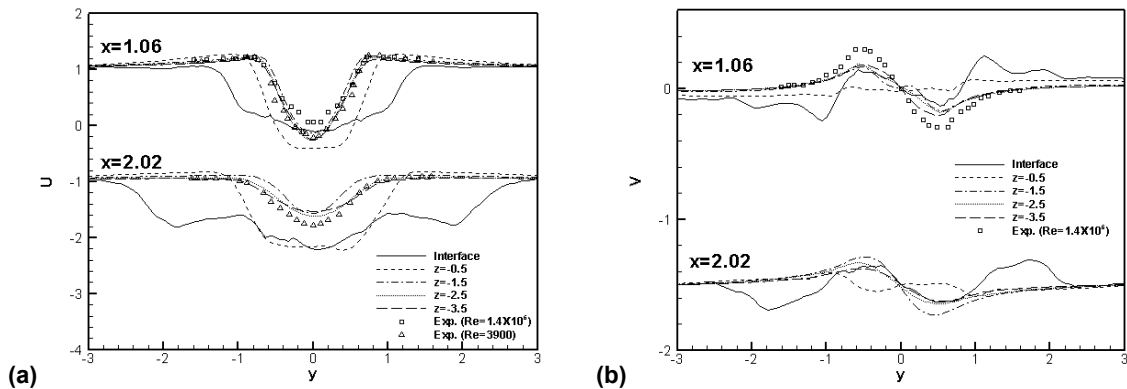


Figure 13 Mean velocity at two locations in the wake of a circular cylinder at $Fr = 0.84$. (a) Streamwise; (b) transverse.

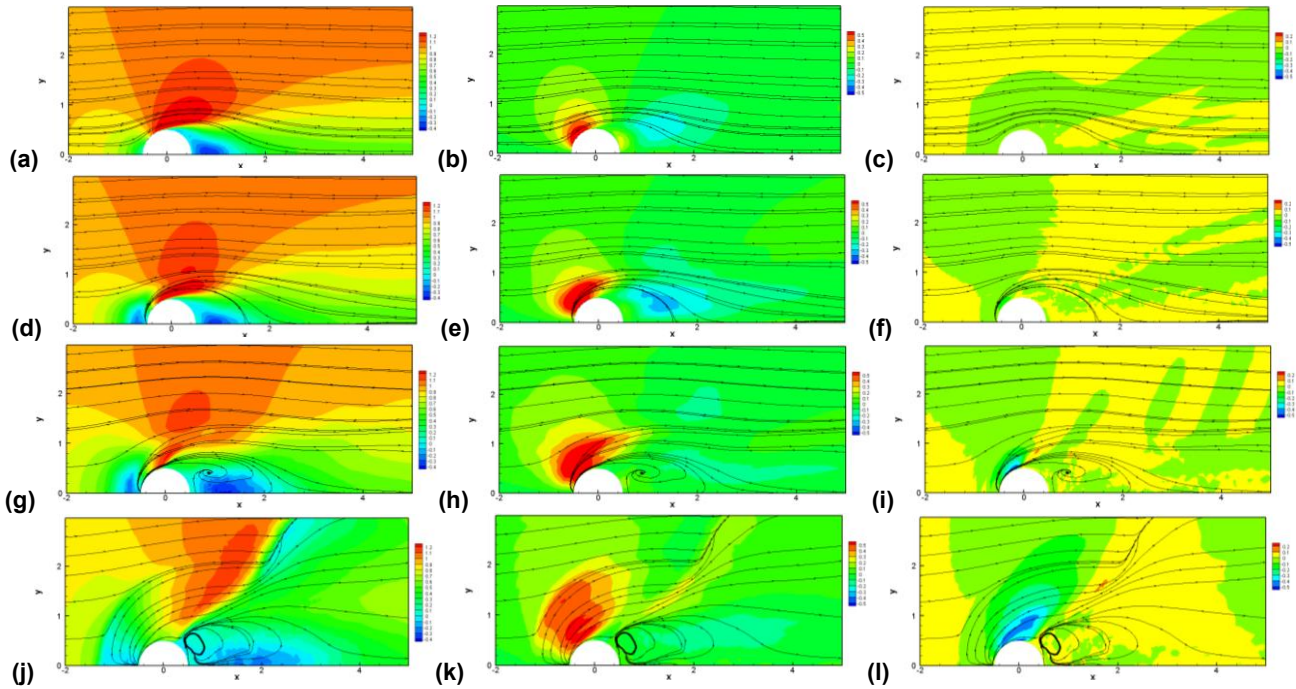


Figure 14 Mean velocity contour at the interface. (a), (d), (g), (j) Streamwise velocity; (b), (e), (h), (k) transverse velocity; (c), (f), (i), (l) vertical velocity for $Fr = 0, 0.20, 0.44,$ and $0.84,$ respectively.

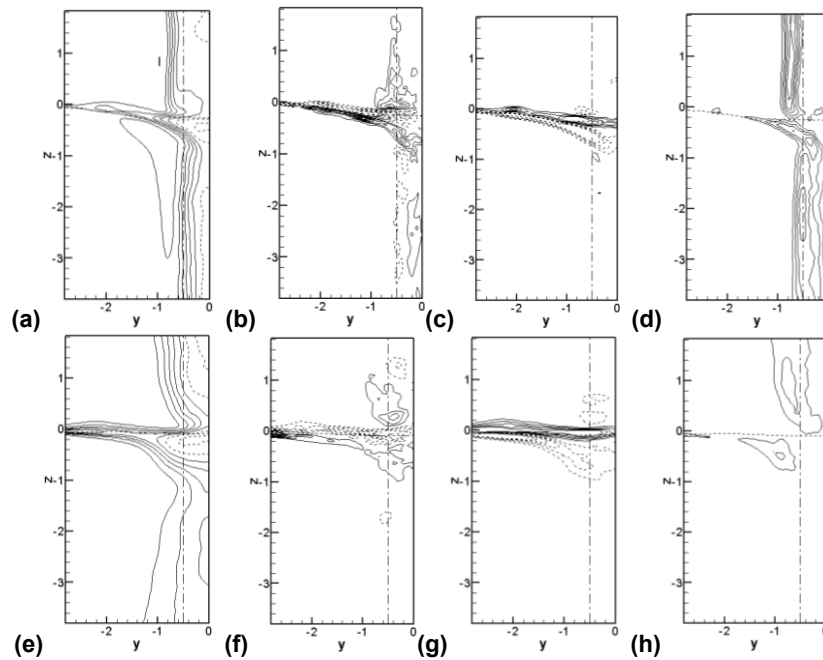


Figure 15 Contours of the mean flow at two cross-stream planes for $Fr = 0.84.$ (a) Streamwise velocity at $x = 1.0;$ (b) streamwise vorticity at $x = 1.0;$ (c) transverse vorticity at $x = 1.0;$ (d) vertical vorticity at $x = 1.0;$ (e) Streamwise velocity at $x = 2.5;$ (f) streamwise vorticity at $x = 2.5;$ (g) transverse vorticity at $x = 2.5;$ (h) vertical vorticity at $x = 2.5.$

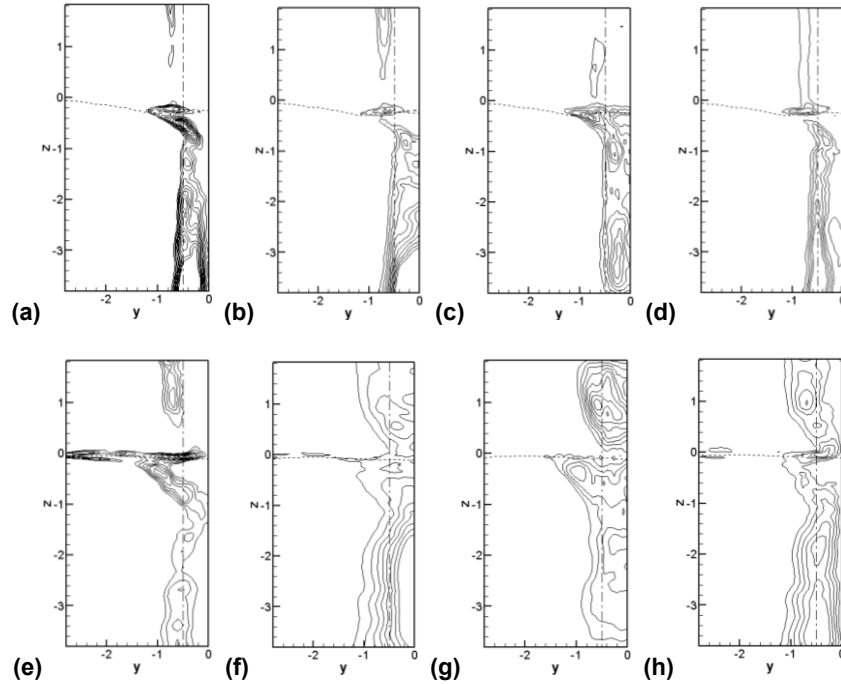


Figure 16 Distribution of the Reynolds stresses at two cross-stream planes for $Fr = 0.84$. (a) \overline{uu} at $x = 1.0$; (b) \overline{vv} at $x = 1.0$; (c) \overline{ww} at $x = 1.0$; (d) \overline{uv} at $x = 1.0$; (e) \overline{uu} at $x = 2.5$; (f) \overline{vv} at $x = 2.5$; (g) \overline{ww} at $x = 2.5$; (h) \overline{uv} at $x = 2.5$.

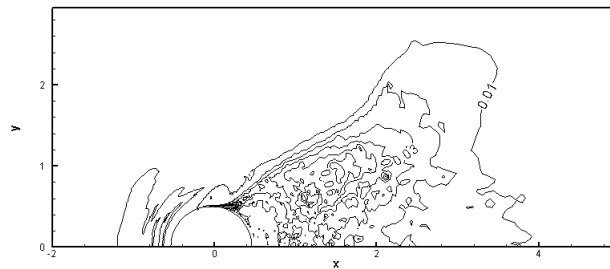


Figure 17 Distribution of the vertical Reynolds stress \overline{ww} at the interface for $Fr = 0.84$

Table 1 Simulation conditions and hydrodynamic forces on the cylinder and run-up

Re_D	Fr_D	Grid and domain size	C_D (EFD)	C_D (CFD)	E (%)	Max y^+	Run-up (Bernoulli)	Run-up (CFD)	E (%)
2.70×10^4	0	$256 \times 128 \times 128$ $40D \times 4D$	N/A	1.28	-	0.96	-	-	-
5.58×10^4	0.20	$256 \times 128 \times 128$ $20D \times 6D$	N/A	1.22	-	0.96	-	0.04	-
1.23×10^5	0.44	$256 \times 128 \times 128$ $20D \times 6D$	1.05 [3] 1.15 [14]	1.1	4.3 -4.7	0.96	0.0968	0.0978	1.0
2.34×10^5	0.84	$256 \times 128 \times 128$ $20D \times 6D$	0.79 [3] 0.89 [14]	0.9	1.1 13	0.96	0.3528	0.355	0.6